Uncovering the toughening mechanisms of bonded joints through tailored CFRP layup

Lima, R. A.A.; Tao, R.; Bernasconi, A.; Carboni, M.; Carrere, N.; Teixeira de Freitas, S.

DOI
10.1016/j.compositesb.2023.110853

Publication date
2023

Document Version
Final published version

Published in
Composites Part B: Engineering

Composites Part B 263 (2023) 110853

Contents lists available at ScienceDirect

Composites Part B

journal homepage: www.elsevier.com/locate/compositesb

Uncovering the toughening mechanisms of bonded joints through tailored CFRP layup

R.A.A. Lima [a,b], R. Tao [b], A. Bernasconi [a], M. Carboni [a], N. Carrere [c], S. Teixeira de Freitas [b,*]

[a] Department of Mechanical Engineering, Politecnico di Milano, Milan, Italy
[b] Faculty of Aerospace Engineering, Delft University of Technology, Delft, the Netherlands
[c] ENSTA Bretagne, UMR CNRS 6027, IRDL, F-29200, Brest, France

ARTICLE INFO

Handling Editor: Prof. Ole Thomsen

Keywords:
CFRP layup Tailoring
Fracture toughness
Secondary bonded joints

ABSTRACT

Aiming to increase damage tolerance of adhesively bonded joints, this work explores the influence of CFRP layup of the adherends on the crack onset and crack propagation of composite bonded joints under mode I loading. Quasi-static Double Cantilever Beam tests were performed using four different CFRP layups bonded with two adhesives. Parallel to the experimental program, finite element analyses were performed to aid in understanding and identifying the various damage mechanisms in each specimen type. The results show that the CFRP layup and adhesive fracture toughness significantly influence the joint fracture phenomena at crack onset and further crack propagation. An enhancement of the joint's mode I fracture toughness values at crack onset was observed in the specimens where a crack competition between the propagation within the bondline and the composite's layers was triggered. During crack propagation, the fracture toughness of the joint increases at crack deflections between the different plies of the CFRP layup until reaching the 0° ply, where sudden delamination occurs. It has been shown that CFRP layup tailoring is a promising toughening method that, when carefully designed, has the potential to increase the maximum effective fracture toughness up to 100% when compared to pure cohesive failure.

1. Introduction

In recent years, global actions have increased to reduce CO_2 emissions and improve sustainability in different industrial fields, and the aeronautical field is not an exception. New solutions are being studied to extend the aircraft's operational life and recycle structural components [1–3]. Moreover, advanced materials such as newly engineered metal alloys and Carbon Fibre Reinforced Polymers (CFRP) have been steadily used to produce lightweight structures and reduce fuel consumption [2].

In order to achieve efficient lightweight structures, the assembly of multi-material and composite components in primary structures is still a key challenge. Adhesive bonding has advantages, such as the negligible negative impact on the substrate's mechanical properties when bonding composite parts, uniform stress distribution, and great design flexibility [2,4]. Nevertheless, the secondary bonding of primary structures is not certified. Adhesive bonding presents limited resistance to crack growth and the risk of sudden failure (especially in aggressive environments) [5–7]. In addition, it remains a challenge to detect interfacial failure caused by weak bonds using the current Non-Destructive Techniques (NDT) and Structural Health Monitoring (SHM) methods [4,8–10]. Therefore, "backup solutions" such as rivets and bolts have been currently implemented to avoid catastrophic failure in safety-critical applications [11–13].

A solution to overcome these limitations and improve the adhesively bonded joint's safety and reliability during their operational life in critical load-bearing applications is to improve the joint's resistance to crack growth, i.e., its fracture toughness. Several methods are proposed in the literature to increase the fracture toughness of composite adhesively bonded joints. Some of these toughening mechanisms are described below.

- Interfacial adhesion patterning over the substrate's surface – is an extrinsic toughening method based on the intentional modification of the interfacial adhesion properties by applying different surface treatments such as pulsed laser irradiation, sandblasting [14], U.V. radiation and plasma [3,15,16] that can trigger bridging mechanisms within the adhesive layer, or by introducing non-sticky Teflon films [17] to tailor sacrificial cracks within the bondline;

* Corresponding author.
E-mail addresses: R.DeAraujoAlvesLima@tudelft.nl (R.A.A. Lima), S.TeixeiraDeFreitas@tudelft.nl (S. Teixeira de Freitas).

https://doi.org/10.1016/j.compositesb.2023.110853
Received 12 March 2023; Received in revised form 12 May 2023; Accepted 13 June 2023
Available online 14 June 2023

- Improvement of the adhesive's mechanical properties – is an intrinsic method based on modifications of the adhesive material by using different curing times [18] or adding micro/nanoparticles (i.e. Carbon Nano Tubes – CNT and Polyhedral-Oligomeric -Sil-Sesquioxanes - POSS) [19–24]. These can either be applied in the complete bondline or in specific regions of the adhesive layer (graded adhesive joints) to architect different mechanical properties throughout the adhesive's length [25];
- Introduction of crack stoppers within the adhesive layer – such as using Z-pinning [7], substrate corrugation, exposing fibres [25,26], and incorporation of woven mats [27] to arrest the crack propagation or adding 'stop holes' ahead of growing crack to reduce the stress singularities in its tip and further delay the crack growth.

Limited research shows how the composite substrate layup can affect fracture toughness. For pure composite laminates without material bondline, the effects of different interface ply orientations on the crack paths were intensively investigated in previous work [28–30]. However, the contributions of laminates' thickness or local orientation in adhesive joints are limited in the literature [11,31–33].

Kupski et al. [11] used different composite ply thicknesses in bonded SLJ. They concluded that thinner composite plies in the substrates showed multiple transverse matrix cracks, leading to a crack deflection from the bondline to the laminates. This resulted in an increase in the energy dissipation and the load at the crack onset (initiation). The ply orientation also played a significant role in increasing joint failure strength [31–33], and it could enhance the joint's fracture toughness associated with the co-occurrence of many damage mechanisms, such as crack branching and deflection [33].

Nevertheless, there is no agreement on which fracture mechanisms can trigger toughening when using composite layup tailoring, nor the role of adhesive toughness in this phenomenon.

This work aims to analyse how CFRP layup can trigger toughening mechanism of adhesively bonded joints and how the adhesive fracture toughness plays a role in the possible enhancement of the joint's fracture toughness both at crack onset and further crack propagation.

2. Materials and methods

2.1. Specimens manufacturing

The unidirectional carbon fibre prepregs Hexply 8552 – AS4 toughened epoxy resin (Hexcel Composites, Cambridge, UK) was used as a substrate material to produce the DCB specimens. Table 1 lists its main mechanical properties.

Aiming to study the influence of the laminate's staking sequence on the joint's fracture toughness, five different layups were manufactured: $[0]_8$, $[0/90_2/0]_S$, $[90/0_2/90]_S$, $[90/45/-45/0]_S$ and $[90/60/90/-60/0]_S$. Table 2 lists the laminate's longitudinal bending stiffness determined through the flexural engineering constant of the laminate (Eq. 01) based on the classical laminate theory.

$$E_x^f = \frac{12}{D_{11}^* t^3} \tag{1}$$

Table 1
Materials properties of Hexply 8552 – AS4 [34].

Longitudinal tensile strength	X_T	2207 MPa
Longitudinal compressive strength	X_C	1531 MPa
Transverse tensile strength	Y_T	81 MPa
Longitudinal tensile modulus	E_{11T}	141 GPa
Transverse tensile modulus	$E_{22T} = E_{33T}$	10 GPa
In-plane shear modulus	$G_{12} = G_{13}$	5.2 GPa
Transverse shear modulus	$G_{23} = E_{33T}/(2(1+\nu_{23}))$	3.33 GPa
In-plane shear strength	$S_{12} = S_{13}$	114 GPa
In-plane Poisson's ratio	$\nu_{12} = \nu_{13}$	0.27
Transverse Poisson's ratio	ν_{23}	0.5

Table 2
Layup stacking sequence and equivalent longitudinal bending stiffness.

Stacking sequence	Equivalent longitudinal bending stiffness, E_x^f (GPa)
$[0]_8$	141
$[0/90_2/0]_S$	88.2
$[90/0_2/90]_S$	63.5
$[90/45/-45/0]_S$	22.2
$[90/60/90/-60/0]_S$	12.8

In Equation 01, D_{11}^* represents the value of the first row and column of the inverse bending stiffness matrix, and t (the total thickness of the laminate) is defined by the number of plies multiplied by the thickness of each ply ($t_{ply} = 0.148\,mm$– determined based on the total laminate thickness after curing).

The Prepreg were stacked by hand layup with intermediate debulking steps for 20 min in a sealed table under the pressure of around 100 mbar between added layers. The CFRP laminates were then cured in an autoclave on a flat aluminium plate covered with an A4000 high-performance fluoropolymer release film (Airtech International INC., USA) under 7 bars of pressure and 110 °C for 60 min.

After curing, the cured CFRP plates were cut to the DCB substrates' dimensions. On the smooth side of the substrate (surface in contact with the aluminium plate during curing), the surface was then carefully manually sanded (400 grid sandpaper) in a criss-cross pattern and cleaned with a soaked acetone cloth. After that, the surface was exposed to artificial high-intensity U.V. lights in an in-house U.V./Ozone apparatus for 7 min, as described in Refs. [17,30], to remove possible organic contaminants and modify the laminates' surface at a molecular level. It is worth mentioning that the total distance between the U.V. lamps and the laminates' surface was equal to 40 mm, and the adhesive's application was made immediately after the U.V./Ozone treatment.

Two adhesives with distinct fracture toughness were used to bond the composite substrates: the bi-component epoxy Araldite 2015/1 (G_{IC} = 640 J/m^2) [30], supplied by Huntsman International LLC, and the tougher epoxy film adhesive with a knit embedded carrier, AF 163 – 2K, supplied by 3 M Scotch-Weld™ (G_{IC} = 2416 J/m^2) [19]. The specific curing procedure of each adhesive is described in Table 3.

The DCB specimens' dimensions are detailed in Fig. 1. A minimum thickness of 0.3 mm of the adhesive layer was ensured for the specimens bonded with the Araldite 2015/1 by metallic spacers positioned in both extremities of the DCBs bonded, and a minimum thickness of 0.25 mm by the nominal thickness of the carrier embedded in the film adhesive AF 163-2k. Additionally, Teflon tape was used to produce an initial crack length of 30 mm.

Finally, loading blocks were bonded at the specimens' top and bottom surfaces using a bi-component epoxy adhesive Araldite 2012.

2.2. Experimental setup

A Zwick electro-mechanical testing machine with a 1 kN load cell was used to perform the DCB quasi-static tests under mode I loading. A testing speed of 4 mm/min was applied in all tests, as recommended by the standard ASTM D5528-13 [35]. The crack position was tracked during the tests by visual inspection of the specimen's lateral surface using a regular camera. The analysed surface was white painted to improve the picture's contrast and crack-tip visualization. At least four

Table 3
Adhesive's curing description.

Adhesive	Time (minutes)	Temperature (°C)	Pressure (bar)	Method
AF 163- 2K	90	120	3	Autoclave
Araldite 2015/1	60	80	–	Oven

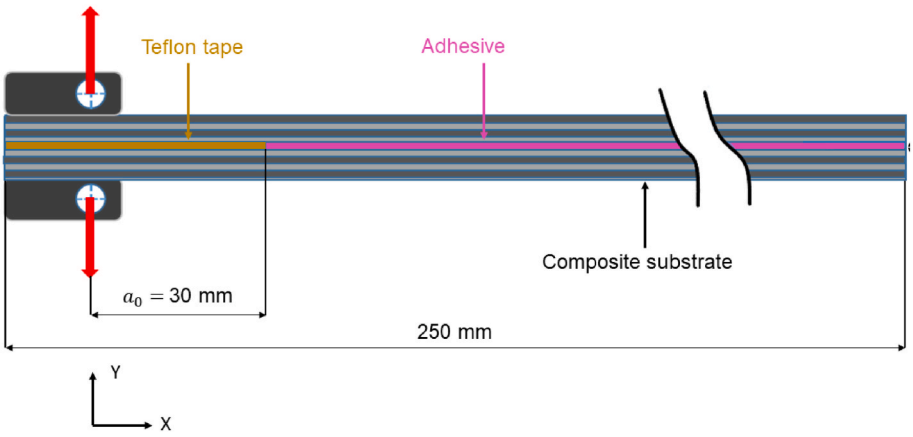

Fig. 1. DCB specimen's dimensions, load conditions and initial crack length.

specimens of each test series were performed.

To better track the crack propagation paths, a travelling microscope was used to take photos of the free lateral surface of the specimen. Both regular and microscope cameras had the photos synchronised with load and displacement information from the testing machine and an acquisition frequency of 4 photos each second. The detailed experimental setup is shown in Fig. 2.

2.3. DCB test – calculation method

The fracture toughness of each specimen was calculated based on the Modified Beam Theory (MBT) data reduction method as recommended by the standards ASTM D5528-13 [35] and ISO 25217 [36].

The following equation was used for this calculation:

$$G_I = \frac{3P\delta}{2b(a+|\Delta|)} * \frac{F}{N} \tag{2}$$

In which P is the load [N], δ is the displacement [mm] recorded by the testing machine during the tests, b and a correspond to the specimen's width and crack length visually measured, respectively. The variable Δ represents a calibration parameter experimentally determined by the intercept of a least squares plot of the cube root of the specimen's compliance ($C^{1/3}$) as a function of the measured crack length, taking the compliance as the ratio between the load-point displacement to the applied load (δ/P). The large-displacement correction (F) and the load-block correction (N) were applied using Equations (3) and (4), respectively.

$$F = 1 - \frac{3}{10}\left(\frac{\delta}{a}\right)^2 - \frac{3}{2}\left(\frac{l_1\delta}{a^2}\right) \tag{3}$$

$$N = 1 - \left(\frac{l_2}{a}\right)^3 - \frac{9}{8}\left[1 - \left(\frac{l_2}{a}\right)^2\right]\frac{l_1\delta}{a^2} - \frac{9}{35}\left(\frac{\delta}{a}\right)^2 \tag{4}$$

In Equations (3) and (4), l_1 is the distance from the centre of the loading point to the mid-plane of the substrate arm to which the loading block is attached and l_2 is the distance between the centre of the loading point to the block edge.

2.4. X-ray micro CT

Selected DCB samples were observed through an X-ray micro CT scanner (Phoenix Nanotom, Waygate Technologies, Germany). Before scanning, the selected DCB samples were loaded, and the opening arms were fixed using a metallic insert to keep them opened for ex-situ observations. The reconstructed 3D model had a voxel size of 12.5 μm.

2.5. Finite element model

A 3D finite element model was created based on continuum Cohesive Zone Elements (CZE), aiming to understand the damage mechanisms triggered by the different layup configurations and mimic their crack propagation paths. For that, the commercial ABAQUS software version 2020 was used.

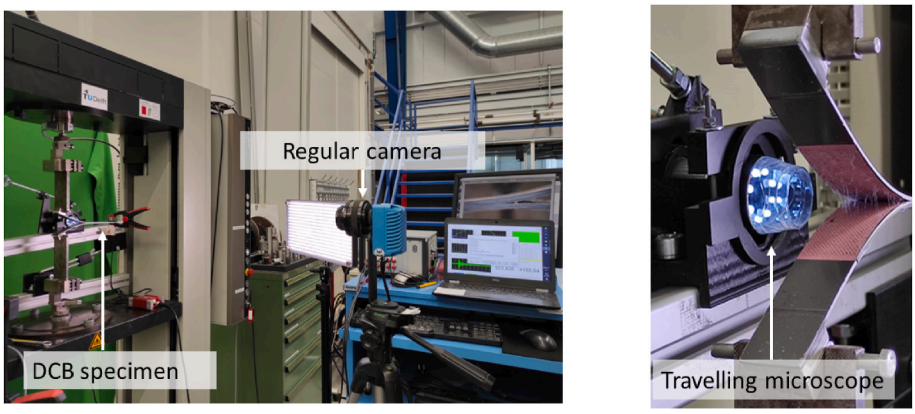

Fig. 2. (a) Experimental setup DCB tests and (b) detail showing the travelling microscope and a specimen $[0]_8$ bonded with adhesive AF 163-2k.

The eight-node brick elements (C3D8) were used to model the CFRP substrate and adhesive materials. The cohesive failure within the adhesive layer, the composite delamination between the composite plies and the matrix cracking within each composite ply were simulated using the eight-node three-dimensional cohesive elements (COH3D8). It is worth mentioning that no distinction is made between the adhesive and the cohesive failure in the adhesive joint. A bi-linear traction separation law was implemented into the model to predict crack growth and degradation based on the maximum nominal stress criteria.

The properties of the materials used in the finite element analysis are described in Tables 4 and 5. The proposed values are based on the materials' data sheet at room temperature (25 °C). It is worth mentioning that a stiffness value of 10^6 was applied for the cohesive elements to avoid elements degradation in undesired regions, as recommended in Refs. [37,38].

Fig. 3 shows an example of the cohesive element layers distribution in the $[90/0_2/90]_s$ specimen. As can be seen, three different cohesive layers with a very thin thickness (5 μm) were created: The first one (pink colour) is located in the middle of the bondline representing a purely cohesive failure (1); the blue lines represent the delamination between the composite plies being located at the interface of each composite ply in the longitudinal direction (2); the green lines are located in the transversal direction of the 90° degree plies, next to the crack tip region to simulate transversal matrix cracking (3). It is important to note that, for the sake of simplicity, the cohesive element has only been introduced in the first 90° ply. In fact, the objective here is to study the competition between the propagation of the crack in the adhesive and the creation of a new crack in the composite.

A mesh convergence study was performed to identify an ideal mesh size that guaranteed mesh-independent results with minimum computational efforts. For the convergence study, two parameters were considered Von Mises stresses and Maximum strain energy release rate. A mesh size of 0.5 mm near the crack tip and 1 mm near the loading point was implemented, with around 145000 elements and 166000 nodes in total.

Fig. 4 shows the boundary and loading conditions of the model, which consisted of on the specimen's right-hand side (Reference Point – RP1), the 3° of freedom were set to zero (encastre) and on the specimen's left-hand side (Reference Point – RP2 and RP3) a constant vertical displacement in its free end (the other degrees of freedom were kept equal to zero).

3. Experimental results

Fig. 5 shows representative load versus displacement curves of the DCB specimens bonded with the AF 163-2k -Fig. 5(a) and Araldite 2015/1 - Fig. 5(b) for the five CFRP layups. The maximum load value before crack propagation was observed in the 0-degree unidirectional specimens (black line) for both adhesive types, approximately 140 N and 50 N for the AF 163-2k and Araldite 2015/1, respectively.

Observing the load versus displacement curves, it is also worth mentioning that the initial stiffness of the curves is different for all specimens due to the different bending stiffness of the layups (see Table 2). As expected, the steepest slope in the linear response region corresponds to the layup with the highest longitudinal bending stiffness $[0]_8$, followed by the $[0/90_2/0]_s$ and $[90/0_2/90]_s$ with lower slopes. The joints with the $[90/45/-45/0]_S$ and $[90/60/90/-60/0]_S$ layups present the lowest stiffness and considerably reduced maximum load values.

Table 4
Material properties used solid elements in the finite element analysis.

Material	E_{11} (MPa)	E_{22}.E_{33} (MPa)	V_{12} - V_{13}	V_{23}	G_{11}- G_{22} (MPa)	G_{33} (MPa)
Hexply 8552 – AS4[a]	141000	9750	0.267	0.5	5200	3190
Adhesive layer	15000	–	0.45	–	–	–

Table 5
Properties used in the cohesive zone elements at the interfaces applied in the finite element analysis.

Material	K (N/mm^3)	G_{Ic} (J.m^{-2})	σ (MPa)
Hexply 8552 – AS4	1.0E6	500[a]	64[a]
Araldite 2015/1	1.0E6	500[b]	22[c]
AF 163- 2K	1.0E6	2416[d]	46[e]

[a] Technical data sheet Hexply 8552 – AS4 [34].
[b] Technical data sheet Araldite 2015/1 [39].
[c] N. P. Lavalette et al. [40].
[d] S. T. de Freitas et al. [17].
[e] J. Kupski et al. [11].

The specimens bonded with the tougher adhesive, AF 163-2k, showed significant differences in the post-peak responses for each type of substrate's CFRP layup, indicating different fracture mechanisms. Fig. 6 shows the representative fracture surfaces for each layup. All specimens AF163-2K_$[0]_8$ presented a cohesive crack propagation within the bondline that gradually decreased the load versus displacement curve after the maximum load – see Fig. 5 (a). All the remaining layups presented a fracture surface within the composite substrate, mostly delamination. In most cases, this led to a sudden drop in load values, except for [90/60/90/-60/0]s layup.

Overall in this particular adhesive, when the interface ply angle was larger than 0-degrees, the crack path deflected (by crack kinking or the initiation of a new crack in the adjacent ply) from the bondline into the composite until encountering the first 0-degree ply, where the crack propagated further by delamination. This was also observed by Kupski et al. [38] in single-lap bonded joints and by Khan et al. [30] in double-lap and flat-wise tensile joints.

As shown in Fig. 6, the crack deflection through the composite for the specimens with $[90/45/-45/0]_s$ and $[90/60/90/-60/0]_S$ layups is even more evident as the crack migrates until the midplane of the composite substrate (crack depth from 1st to 4th and 5th layers, respectively). Due to the crack path deflection into the laminate, the opening of DCB specimens was no longer symmetric, leading to a twisting curvature of bonded CFRP parts.

Fig. 7 shows the representative fracture surfaces of the specimens bonded with Araldite 2015/1. The layups $[0]_8$, $[0/90_2/0]_S$, and $[90/0_2/90]_S$ showed cohesive failure and similar trends of the load versus displacement curves with a gradual decrease of the load after the maximum value.

For specimens with $[90/45/-45/0]_S$ and $[90/60/90/-60/0]_S$ layups, the crack deflected into the composite substrate until reaching the 0-degree ply delamination - identically to what was observed with the adhesive AF 163-2K. It is worth mentioning that for the specimens bonded with the Araldite, the specimen $[90/45/-45/0]_S$ actually presented lower stiffness when compared with the [90/60/90/-60/0]s specimen, conversely from what was calculated and present in Table 2. A possible reason for this behaviour is the crack onset of the Araldite_$[90/45/-45/0]_S$ within the bondline (see Fig. 7), followed by crack deflection into the composite substrate, that was not present in the AF163-2K_$[90/45/-45/0]_S$.

It is worth mentioning that the high opening displacement observed during the tests changed the testing conditions from pure cleavage to peel/cleavage conditions. This peel/cleavage condition was more severe in the specimens with lower bending stiffness, as in the layups with 45 and 60-degree plies orientation. In addition, the increasing peel stresses locally increased the stress concentration at the substrate's leading edge. They affected the crack competition phenomenon and might have influenced the crack deflection in the composites with higher fibre orientation angles.

Fig. 8 shows the R-curves for each corresponding load versus

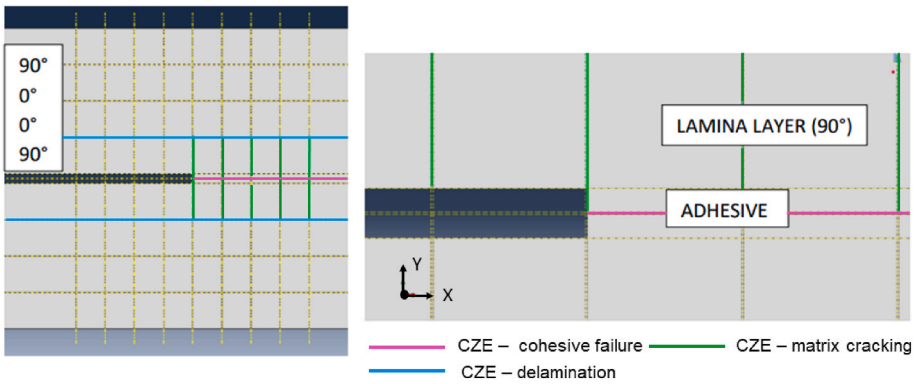

Fig. 3. Example of the cohesive zone elements (CZE) distribution in $[90/0_2/90]_s$ finite element analysis: (1) pink lines CZE representing cohesive; (2) blue lines CZE representing delamination and (3) green lines CZE representing the transverse matrix cracking. (For interpretation of the references to colour in this figure legend, the reader is referred to the Web version of this article.)

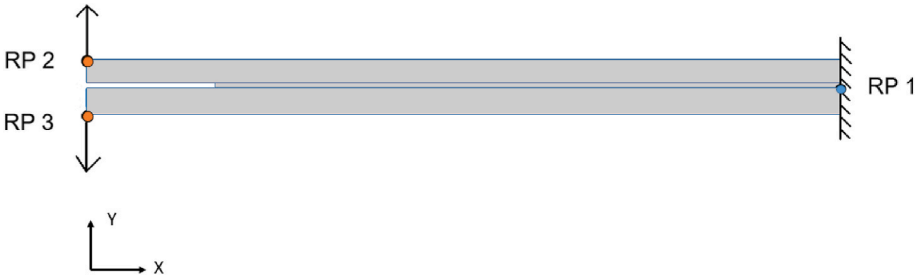

Fig. 4. Scheme boundary conditions numerical model.

displacement curve presented in Fig. 5. The fracture toughness of the DCB joint was determined by Equation 02 as recommended by the standards ASTM D5528-13 and ISO 25217. Table 6 presents two values of the fracture toughness: Onset G_{eff} representing the point in the R-curve where the crack propagation was first visually observed, and Max G_{eff} representing the max G_{eff} value achieved during crack propagation (complete R-curve).

As seen in Fig. 8 (a), the effective energy release rate of the AF 163-2k_$[0]_8$ unidirectional joint (black line) is stable but increases during crack propagation as a function of the crack length, as also observed in Ref. [41]. The fracture toughness at onset value is 2941 J/m^2. This is approximately 20% higher than the value of the fracture toughness at onset reported by Ref. [17] for the same adhesive and 52% higher than for the same adhesive without a carrier (AF163-2U – unsupported, G_{eff} = 1924 J/m^2), reported in Ref. [42]. For the AF163-2k_$[0/90_2/0]_S$ and AF163-2k_$[90/0_2/90]_S$ specimens, a high peak characterises the beginning of the R-curve (maximum G_{eff} equals to 3250 and 1921 J/m^2, respectively) followed by a sudden drop in the G_I value to a plateau around 300 J/m^2 as the crack propagates. Of particular interest is the AF163-2k_$[0/90_2/0]_S$ joint's fracture toughness peak (Max G_{eff} = 3250 J/m^2), which is 10% higher than the one shown in the unidirectional specimen AF163-2k_$[0]_8$ at the onset region (onset G_{eff} = 2941 J/m^2). Further analysis of the reason behind this improvement is described in the discussion section.

Fig. 8 (b) shows the R-curve using Araldite 2015/1 – a low-toughness adhesive. A stable crack propagation is observed in the specimens with cohesive failure within the bondline, i.e., Araldite_$[0]_8$, Araldite_$[0/90_2/0]_S$ and Araldite_$[90/0_2/90]_S$. The average value fracture toughness measured in these specimens is 590 J/m^2, which is in accordance with Araldite 2015/1 nominal fracture toughness specified by the supplier (between 400 and 600 J/m^2) [38].

For both adhesives, the R-curves of the $[90/45/-45/0]_S$ and $[90/60/90/-60/0]_S$ specimens have a wavy shape (peaks and valleys before the plateau) which will be discussed in more detail in section 5. It is out for notice that the $[90/60/90/-60/0]_S$ specimens bonded with the adhesive Araldite 2015/1 present a 37% increase of the fracture toughness onset (Onset G_{eff} = 772 J/m^2) and almost 100% increase considering its maximum fracture toughness (Max G_{eff} = 1120 J/m^2) when compared with the $[0]_8$ specimens (onset G_{eff} = 563 J/m^2).

It is worth mentioning that for the Araldite_$[0]_8$, Araldite_$[0/90_2/0]_S$ and Araldite_$[90/0_2/90]_S$ specimens, the R-curve is very stable, and the maximum G_{eff} values are within the onset G_{eff} standard deviation.

Table 6 also presents the Δ values for each specimen type calculated from the intercept of a least squares plot of the cube root of the specimen's compliance ($C^{1/3}$) as a function of the experimentally measured crack length. In this study, the Δ does not represent only a calibration parameter to account for the specimens' root rotation. Instead, it gives additional information related to the fracture process zone and damage evolution phenomena within the specimens, as stated in Ref. [42]. Mainly for the specimens with a cohesive failure, the Δ values can represent the extension of the fracture process zone length (around 10 to the failing cohesively in the Araldite 2015/1).

Even though not-pure mode I crack propagation was observed in the specimens where a crack deflection to the composite layup and further delamination was undertaken, the Δ values could also provide insights about the specimens' damage development. For the specimens where the crack propagated through the composite layers, smaller Δ values were determined, representing a short damaged zone area ahead of the crack tip and probably more brittle behaviour of the composite matrix compared with the adhesive.

It is worth pointing out that for the specimens with the 45 and 60-degree layups, the crack propagation was no longer symmetric and simultaneous multi-cracks were triggered. As a result, the crack lengths measured on each side of the specimen are not the same. Therefore, different $C^{1/3}$ versus the crack length curves would be expected as different absolute delta values.

All the least squares plots of the cube root of the specimens' compliance in the function of the crack length were linear and with a

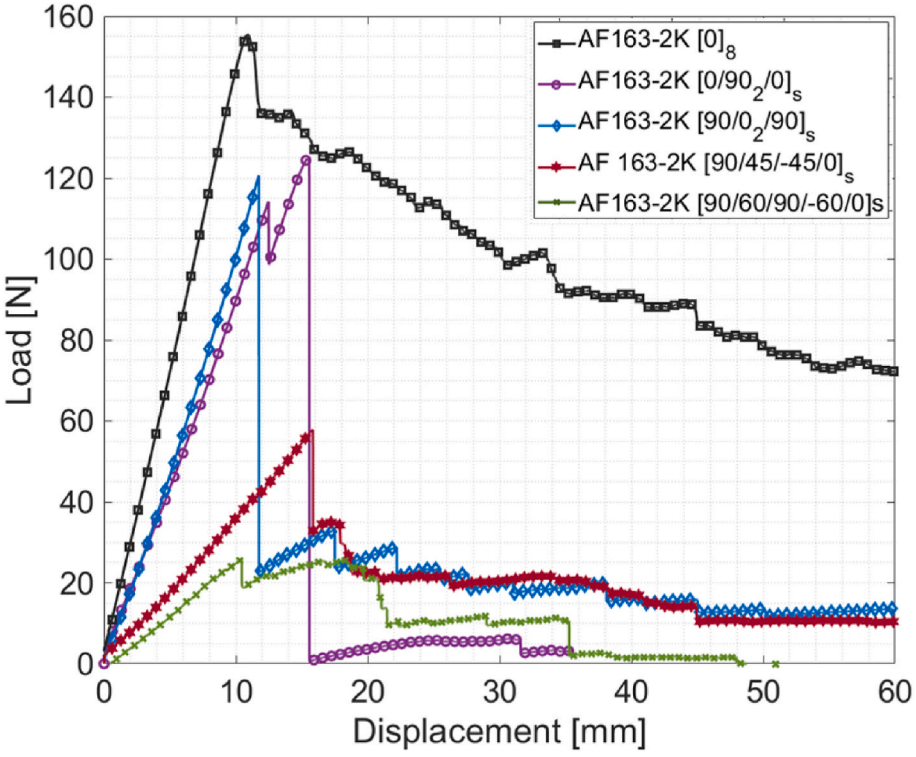

(a)

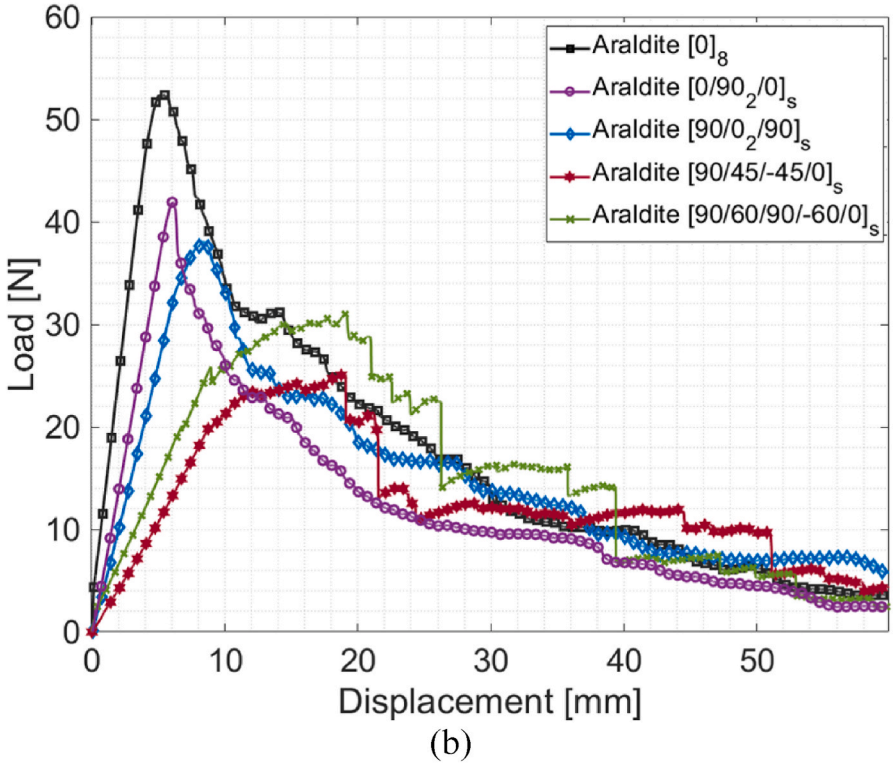

(b)

Fig. 5. Load versus displacement curves (a) AF163-2k and (b) Araldite 2015/1 adhesive.

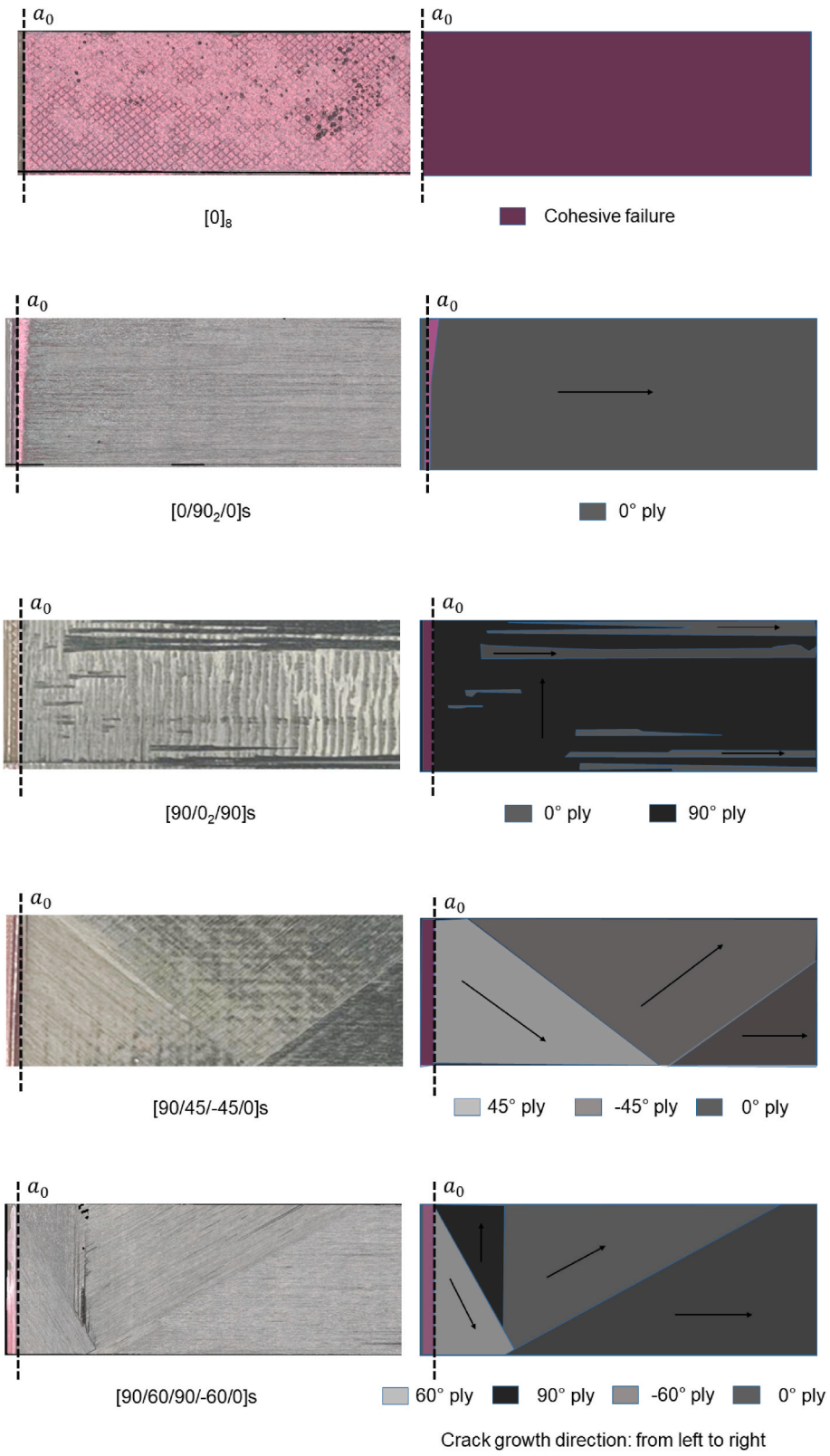

Fig. 6. Representative fracture surface of the AF163-2K DCB specimens (photos on the left-hand side and schematics of the fracture and ply angles on the right-hand side).

constant value for Δ, except for the AF 163-2k_$[0]_8$ specimen. Fig. 9 shows this plot for one representative specimen.

As seen in Fig. 9, the first range of data represented the linear path of the curve (Δ = 7.3). Instead, the second range (Δ = 9.5) showed the transition from the previous linear behaviour by changing its slope. The presence of this second range can be associated with a more significant influence of the carrier bridging in delaying the crack propagation, therefore changing the slope of the $C^{1/3}$ versus the crack length curve.

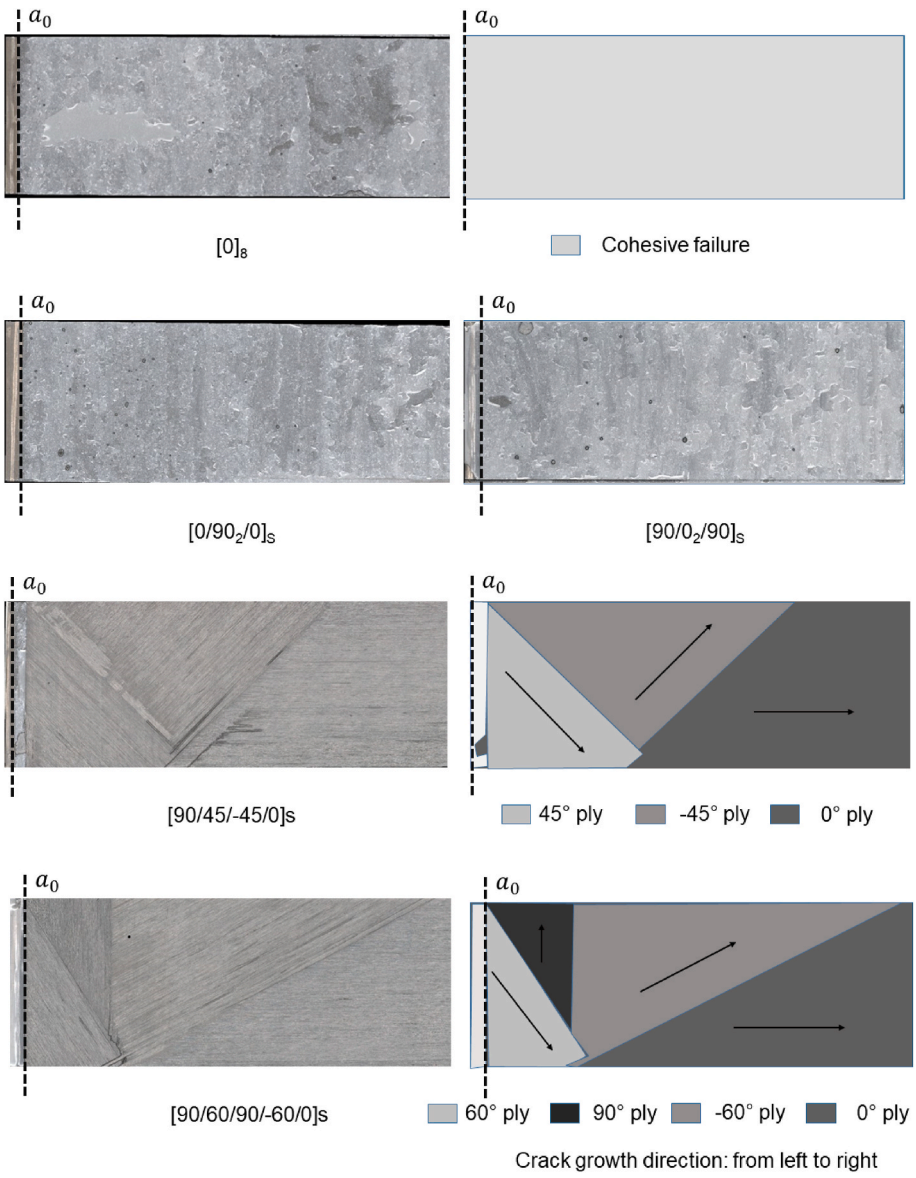

Fig. 7. Representative fracture surface of the Araldite 2015/1 DCB specimens (photos on the left-hand side and schematics of the fracture and ply angles on the right-hand side). In the second row, only photos are shown since both specimens presented a cohesive failure.

Considering that different Δ values will directly affect the fracture toughness calculation, it can limit the accuracy of the MBT method, predominantly when analysing specimens with multiple crack fronts and where bridging phenomena are triggered.

To seek clearness, all the Δ values reported in Table 6 considered the linear regression of all the reported data in the $C^{1/3}$ versus the crack length curve.

4. Numerical results

Another relevant tool to better understand the damage mechanisms within the proposed joints and the different paths undertaken by the crack is the Finite Element Analysis (FEA). A failure criterion based on linear-elastic fracture mechanics was used to predict the crack onset for each studied composite layup. Following this criterion, once initiated, the crack can propagate if the energy release rate is greater than the toughness. Table 7 compares the crack onset location observed experimentally and obtained from the finite element analysis.

For the tougher adhesive AF 163-2K, the adherend layup strongly influenced the joint's G_{eff} onset values since its transversal strength seems competitive compared with the composites. It is worth noticing that the highest fracture toughness at crack onset was achieved when using the layups AF 163-2k_[0]$_8$ and AF 163-2k_[0/90$_2$/0]$_S$.

The Araldite 2015/1 adhesive with lower fracture toughness presents a cohesive failure in most studied cases, showing that the preferential path for crack propagation was the bondline. The Araldite_[0]$_8$, Araldite_[90/0$_2$/90]$_S$, and Araldite_[0/90$_2$/0]$_S$ specimens that presented a cohesive failure present a G_{eff} value of around 590 J/m^2. For the layups with 45 and 60-degree plies orientation where the fracture occurred within the composite substrate, the fracture toughness of these joints was higher than the fracture toughness of the intralaminar CFRP (300 J/m^2) and the cohesive failure of the adhesive Araldite (590 J/m^2).

5. Discussion

To better understand the influence of the composite's layups on the fracture behaviour of composite bonded joints under mode I loading, the crack propagation paths were recorded in detail for each crack increment. The Load and displacement (L-d) curves and R-curves of each test series were then correlated with the crack propagation paths. This

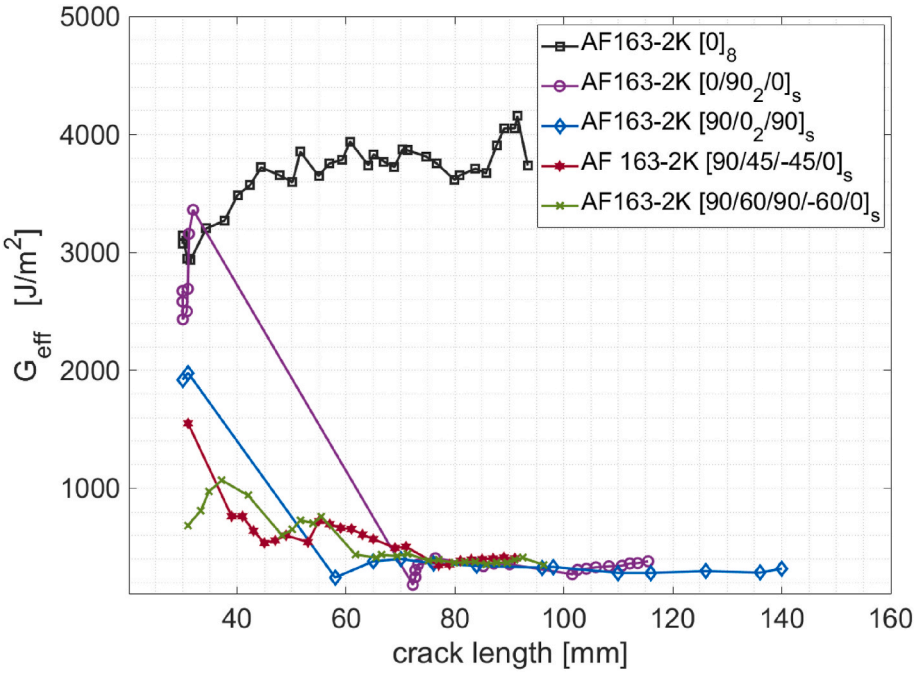

(a)

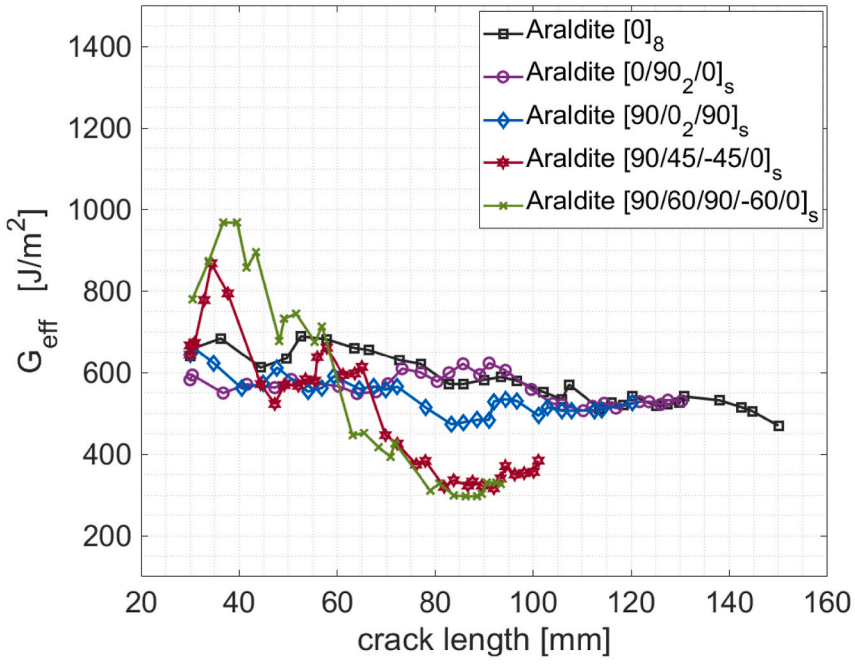

(b)

Fig. 8. R-curve of DCB specimens bonded with (a) AF 163-2k and (b) Araldite 2015/1 adhesive.

discussion section is divided into three main subgroups of laminate: unidirectional laminate, cross plies and multidirectional layups.

5.1. Unidirectional laminate $[0]_8$

As previously observed, all specimens with $[0]_8$ as substrates, AF 163-2k_$[0]_8$ and Araldite_$[0]_8$ presented cohesive failure. The specimens bonded with the Araldite presented a stable and almost constant R-curve with a G_{eff} value of around 540 J/m^2; see Fig. 8(b). However, AF 163-2k_$[0]_8$ presented a linear increase of the R-curve during the mode I crack propagation, as detailed in Fig. 10 (a). Fig. 10 (b) shows the images of the two highlighted points in the R-curve from the travelling digital microscope.

Fig. 10 (b) shows that the cohesive failure of the AF163-2k adhesive and a carrier pull-out was observed throughout the complete crack length. This carrier pull-out resulted in crack bridging and increased the

Table 6
Effective fracture toughness at crack onset (Onset G_{eff}), maximum values achieved throughout the R-curve (Max G_{eff}) and calculated Δ values.

Adhesive type	CFRP stacking sequence	Onset G_{eff} (J/m^2) (average ± standard deviation)		Max G_{eff} (J/m^2) (average ± standard deviation)		Calculated Δ values (mm) (average ± standard deviation)	
AF 163 – 2K	$[0]_8$	2941	±131	3690	±263	10.9	±1.8
	$[0/90_2/0]$s	2958	±233	3250	±124	4.8	±1.2
	$[90/0_2/90]$s	1894	±157	1921	±150	11.8	±2.5
	$[90/45/-45/0]_S$	1343	±154	-[a]		4.4	±2.9
	$[90/60/90/-60/0]_S$	743	±46	1018	±63	0.4	±0.3
Araldite 2015/1	$[0]_8$	563	±49	-[a]		11.6	±0.5
	$[0/90_2/0]$s	611	±27	-[a]		11.2	±0.8
	$[90/0_2/90]$s	597	±65	-[a]		9.9	±1.5
	$[90/45/-45/0]_S$	649	±18	771	±57	1.1	±0.4
	$[90/60/90/-60/0]_S$	772	±125	1120	±170	2.2	±0.5

[a] Max G_{eff} within the same values as Onset G_{eff}.

energy needed to open an increment of the crack as the crack progressed. As a result, the G_{eff} value increased in every crack increment: increasing the joint's fracture toughness from about 3139 J/m^2 in point 1–3939 J/m^2 in point 2 (an increase of around 25% between points 1 and 2).

Fig. 11 shows Micro CT images of one of the DCB coupons. As observed, the carrier bridging occurred throughout the entire specimen width, in which the carrier wires were pull-out from the adhesive layer while the crack propagated. This toughening mechanism occurs behind the crack tip, i.e., only triggered after the crack has propagated. The carrier bridging worked as an extrinsic toughening mechanism of the adhesive joint with an increase of toughness in an average of 16 J/m^2 per crack length unit. A similar extrinsic toughening mechanism was also observed in Ref. [30] with the same type of adhesive.

5.2. Cross-ply laminates $[0/90_2/0]_S$ and $[90/0_2/90]_S$

For the cross-ply laminates, each adhesive presented different results. The specimens bonded with Araldite 2015/1 adhesive presented cohesive failure, as previously observed in Fig. 7, while AF163-2k_$[0/90_2/0]_S$ and AF163-2k_$[90/0_2/90]_S$ specimens presented damage mechanisms mainly characterised by matrix cracking and delamination.

To better understand these differences and the influence of the adhesive's type in the crack propagation paths within the joints, the stiffness degradation of the different CZE (see Fig. 3) is shown in Fig. 12.

It is worth mentioning that the arrows in Fig. 12 represent the crack propagation within the adhesive layer (green colour), the crack deflection through the composite layups (red colour), and the paths with an increase in the cohesive elements' stiffness degradation – regions of stress concentration.

Table 7
Location of the crack onset observed experimentally and obtained by finite element analysis.

Adhesive type	CFRP stacking sequence	Crack onset location (Experimental)	Crack onset location (FEA)
AF 163 – 2K	$[0]_8$	adhesive	adhesive
	$[0/90_2/0]$s	adhesive followed by matrix cracking	adhesive and composite layup
	$[90/0_2/90]$s	composite layup	adhesive and composite layup
	$[90/45/-45/0]_S$	composite layup	composite layup
	$[90/60/90/-60/0]_S$	composite layup	–
Araldite 2015/1	$[0]_8$	adhesive	adhesive
	$[0/90_2/0]$s	adhesive	adhesive
	$[90/0_2/90]$s	adhesive	adhesive
	$[90/45/-45/0]_S$	adhesive and composite layup	adhesive and composite layup
	$[90/60/90/-60/0]_S$	composite layup	–

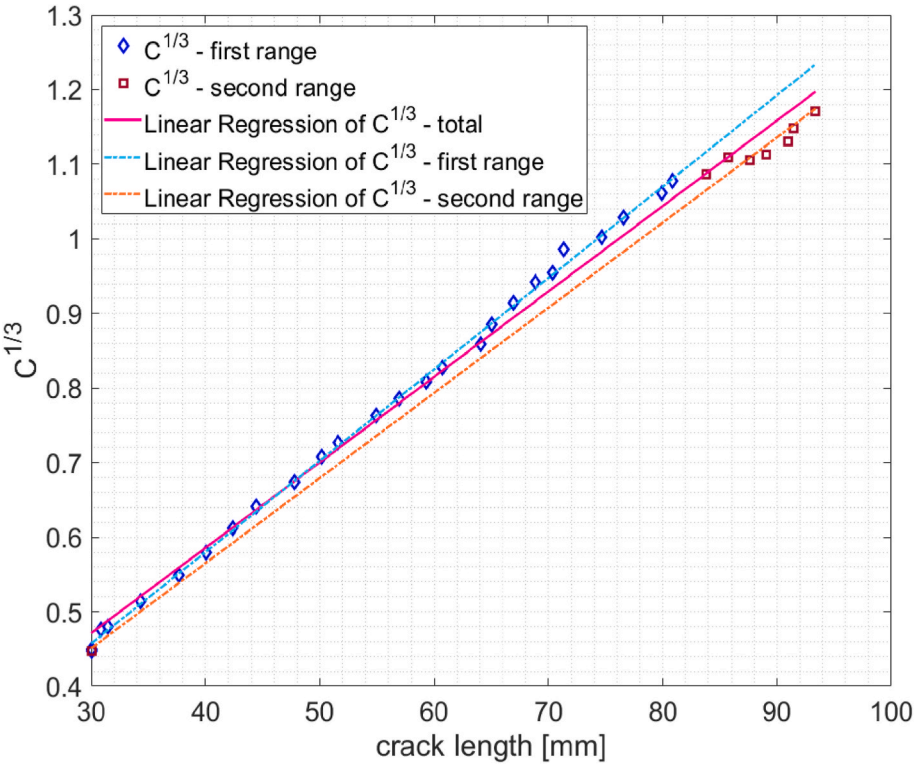

Fig. 9. Representative Δ determination of AF 163-2k_$[0]_8$ specimen.

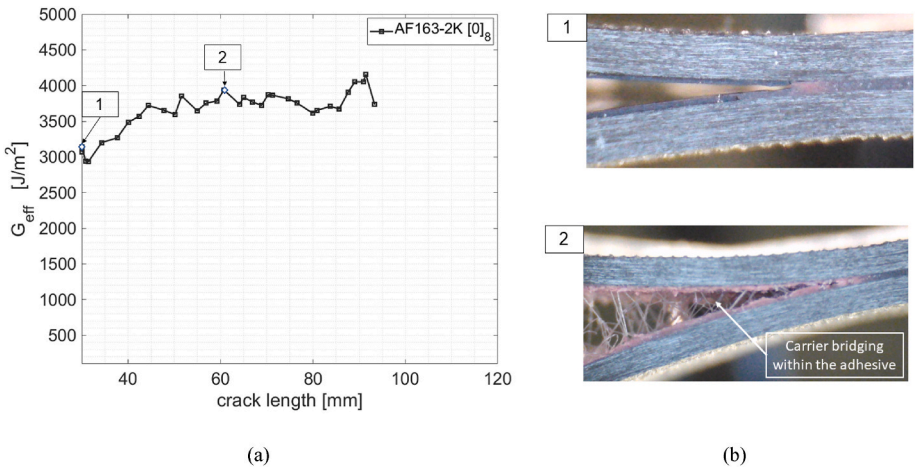

Fig. 10. (a) Detailed R-curve of AF 163-2k_$[0]_8$ specimen and (b) lateral images taken from the travelling microscope in points 1 and 2.

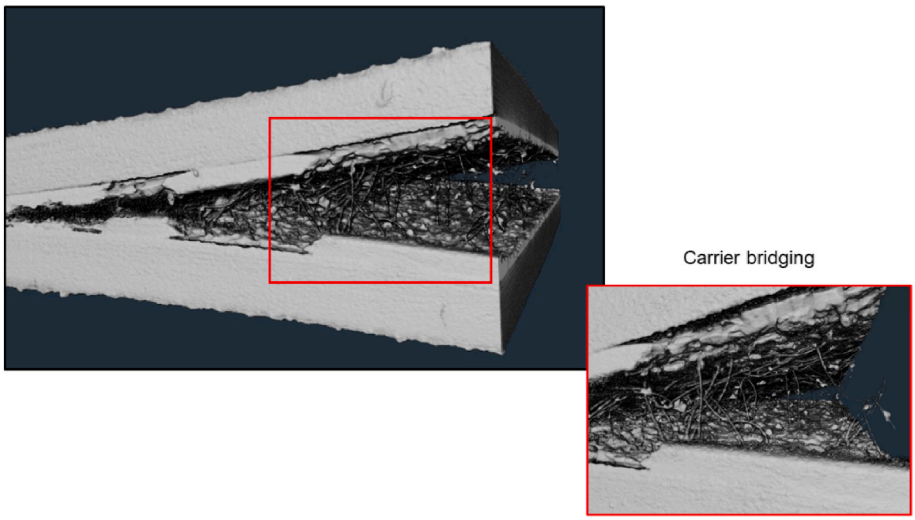

Fig. 11. Micro CT images of specimen AF 163-2k_$[0]_8$.

In the case of the AF163-2K_$[0/90_2/0]_S$ and AF163-2K_$[90/0_2/90]_S$ specimens in Fig. 12 (a) and (c), the mechanism of crack competition is more evident since local stress singularities can be seen in different regions of the laminates' layup (represented by regions with higher stiffness degradation – blue arrows). The crack propagates until the local stresses finally overcome the adhesive's (green arrows) or the laminate's transversal strength (red arrows). So, for these specimens, a co-occurrence of multiple damage mechanisms (i.e., cohesive failure, matrix cracking and delamination) was triggered by the 90/0-degree layup combined with a tough adhesive.

For the $[0/90_2/0]_S$ and $[90/0_2/90]_S$ specimens bonded with the adhesive Araldite 2015/1 (Fig. 12 (b) and (d) respectively), the stresses singularity at the crack-tip of the adhesive is predominant, leading to a cohesive failure onset. It is worth mentioning that the difference between the curing process of the two adhesives during the bonding process could influence the matrix/fibre adhesion of the composite as a post-curing step [16], at least partially, that affects the laminate's transversal strength and consequently the crack competition phenomenon.

Hereby we would like to pay particular attention to the specimens AF163-2K_$[0/90_2/0]_S$ fracture phenomena. This layup resulted in the highest toughness at crack onset, overcoming the crack onset of cohesive failure with $[0]_8$ layup. Fig. 12 highlights four points in the L-d curve and corresponding R-curve to explain the increase in the joint's fracture toughness; see Fig. 13 (a) and (b). Fig. 13 (c) shows the corresponding microscopic images of the region close to the crack tip at those four points.

From the images and correspondent load versus displacement test output of Fig. 13, we can observe that.

1. First peak in the load: No visible damage is yet identified;
2. First sudden decrease in the load: matrix cracking at the 90° plies (the 2nd and 3rd from the bondline) is observed, followed by cracking propagation to the interface between the 0° interface layer (1st ply from the bondline) and the 0° at the symmetry plane (4th ply from the bondline), leading to a z shape crack depicted in Fig. 8 (d) – detail 2;
3. Increasing the load from point 2 to 3: represents the crack competition between the delamination between the 0–90 plies triggered by the matrix cracking and crack propagation inside the adhesive layer, i.e., cohesive failure;
4. A second sudden decrease in the load: delamination within the 0-degree interface ply (next to the bondline).

The fracture phenomena described above lead to an enhancement of approximately 10% at the G_{eff} of AF163-2k_$[0/90_2/0]$s compared with the cohesive failure onset in AF163-2k_$[0]_8$. The composite layup properties, combined with the stress singularities of the pre-existing

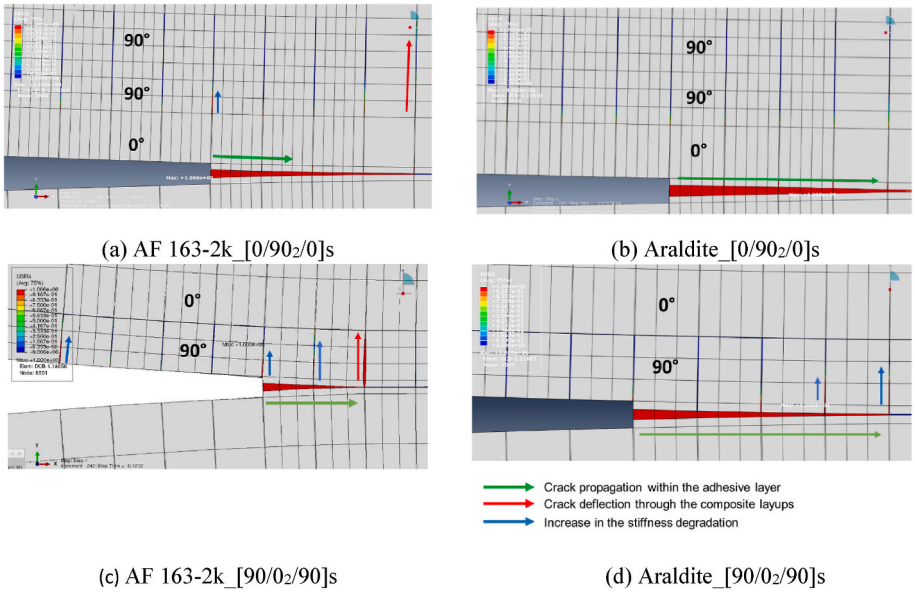

Fig. 12. CZE stiffness degradation predicted by FEA of specimens $[0/90_2/0]$s bonded with adhesives (a) AF 163-2K and (b) Araldite 2015/1; $[90/0_2/90]$s bonded with adhesives (c) AF 163-2K and (d) Araldite 2015/1. (colours transition from blue to red, that is, from undamaged to completely damaged). (For interpretation of the references to colour in this figure legend, the reader is referred to the Web version of this article.)

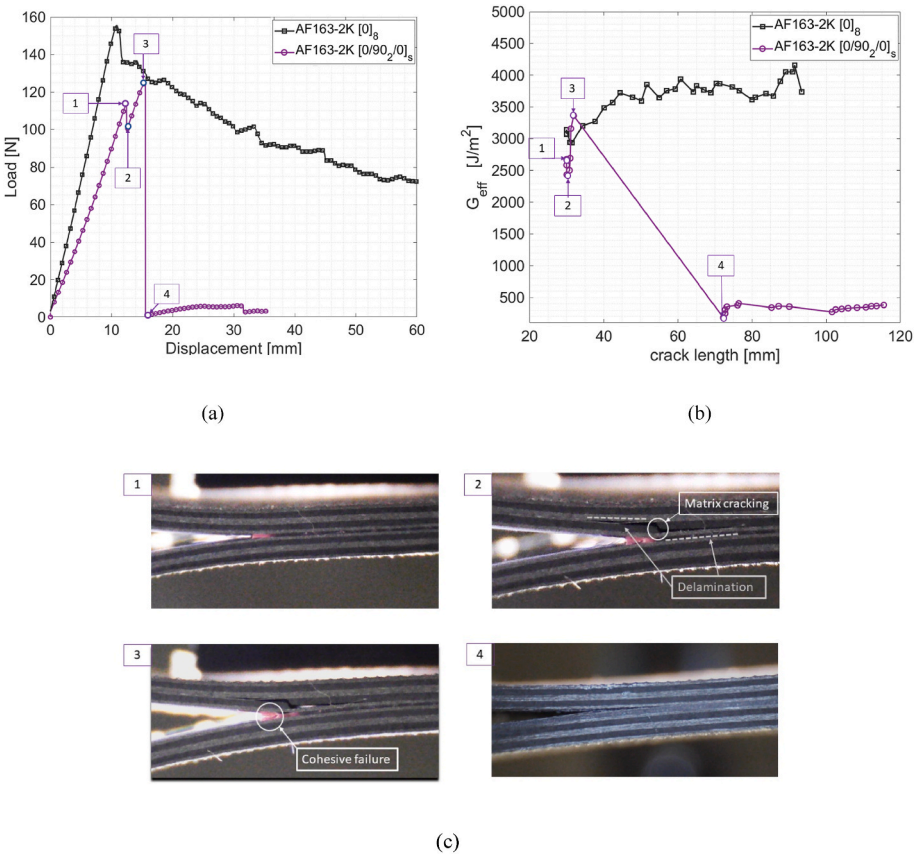

Fig. 13. Detailed crack propagation paths of specimen AF 163-2k $[0/90_2/0]_S$ and $[0]_8$ and corresponding points at the load versus displacement and R-curve.

crack tip, lead to a crack competition phenomenon at the fracture onset in which multi-damage mechanisms co-occur, from matrix cracking to cohesive failure and crack deflection to the 0–90° interface ply.

Higher energy is therefore required to overcome this competition until a more energetically favourable crack path is pursued. In this specific case, the delamination at the 0-degree ply and, consequently, reduced G_{eff} values.

Fig. 14 shows the topography images of the final fracture surface of the AF163-2K_$[0]_8$ and AF163-2k_$[0/90_2/0]_S$ specimens with a colour scale from 0 to 1 mm, performed using the Keyence VR 5000 wide-area 3D profiling system. The lower limit (zero value) was defined based on the free surface of the specimen (without adhesive) and is defined as the

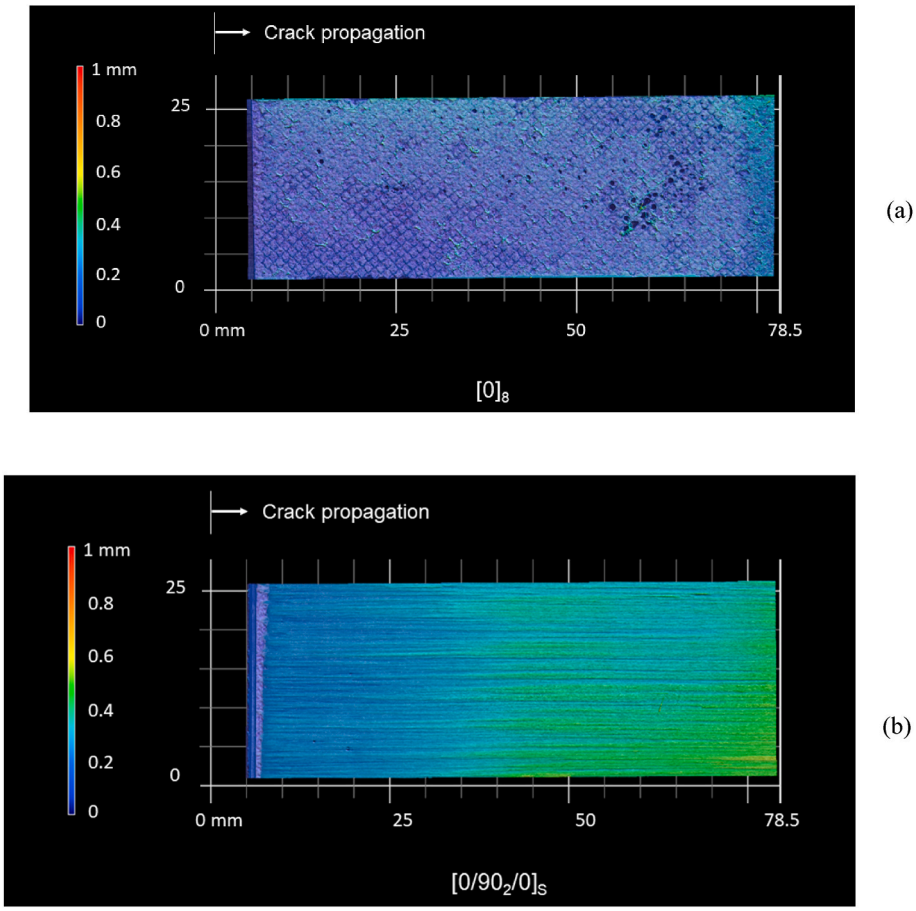

Fig. 14. Topography of the fracture surface of specimens (a) AF163-2k_$[0]_8$ and (b) AF163-2k_$[0/90_2/0]_S$.

baseline for all specimens. As can be observed in Fig. 14 (a), the cohesive failure of specimen AF163-2k_$[0]_8$ is almost on the adhesive midplane, represented by the almost uniform dark blue colour. For AF163-2k_$[0/90_2/0]_S$ in Fig. 14 (b), it is possible to see clearly a tiny region (violet colour) that represents a small propagation within the adhesive layer, followed by a delamination in the 0° ply, confirming the observations took during the analyses of the images of the travelling microscope.

5.3. *Multidirectional laminates $[90/45/-45/0]_S$ and $[90/60/90/-60/0]_S$*

For the multidirectional laminates, two main observations will be hereby discussed. The first is the reasoning behind the wavy shape observed in the R-curve of both multidirectional laminates in both adhesives – see Fig. 8. The second one is the influence of the adhesive type on the different crack onsets observed for the specimens with 45-degree ply – see Table 6.

Figs. 15 and 16 show the R-curve, the images from the lateral of the specimens taken by the travelling digital microscope and the topography images of the fracture surfaces for the specimens Araldite_$[90/45/-45/0]_S$ and Araldite_$[90/60/90/-60/0]_S$, respectively.

Fig. 15 (a) shows an increase in the G_{eff} values between points 1–2 and 3–4. By analysing the fracture surfaces a posteriori (Fig. 15 (b), these peaks represent a transition between the crack propagation paths within the joint. It is also possible to identify a crack deflection between 90 and 45-degree plies (point 2) and transition between 45, and 45 and 0-degree plies (close to point 4), followed by a decrease representing the crack deflection to the 0-degree ply and final delamination (almost constant G_{eff} values) in point 5. A similar trend was also observed in the $[90/60/90/-60/0]_S$ specimens, with the peaks in points 2 and 4 that represent the transition regions between multiple fracture surfaces, in particular 60 to 90 and -60 in point 2 and from −60 to 0°.

From images of the travelling microscope (mainly in Fig. 15 (c), details 3 and 4, and 16 (b), details 2 and 3), conversely to the other stacking sequences, the crack propagated simultaneously in different plies. This phenomenon is probably driven by the specimens twisting due to the asymmetry promoted in the specimens' adherends since the crack keeps propagating through the composite's thickness [43,44]. As stated by Khan [28] and Kupski [11,37], in joints with higher fibre orientation angles next to the adhesive layer, the crack tends to propagate further inside the composite due to increased peel stresses in the layups neighbouring.

Moreover, Figs. 15 (b) and 16 (b) confirm that the crack propagated simultaneously in different plies at various crack positions. In Fig. 15 (b) at point 3 (between 20 and 25 mm), the crack propagated in both + and −45° plies (confirmed by the different colours graduation, meaning different planes within the joint), staying stable only when the 0° degree ply was reached. Similar behaviour can also be observed in the Araldite_$[90/60/90/-60/0]_S$ specimen, where a crack deflection from the 60°, 90° and −60° plies could be observed within the first 25 mm of propagation.

Micro CT images of the Araldite_$[90/60/90/-60/0]_S$ specimen were taken during the DCB test, as shown in Fig. 17. It is possible to see several crack propagation fronts in multiple composite plies happening simultaneously. These multiple crack fronts can not be identified purely by the side image of the specimen.

Fig. 17 shows the CZE stiffness degradation in the FEA of AF 163-2k_[90/45/-45/0]s and Araldite_[90/45/-45/0]s.

In Fig. 18 (a) of the AF163-2k_$[90/45/-45/0]_S$ specimens, no stiffness degradation was identified in the bondline, indicating that the local

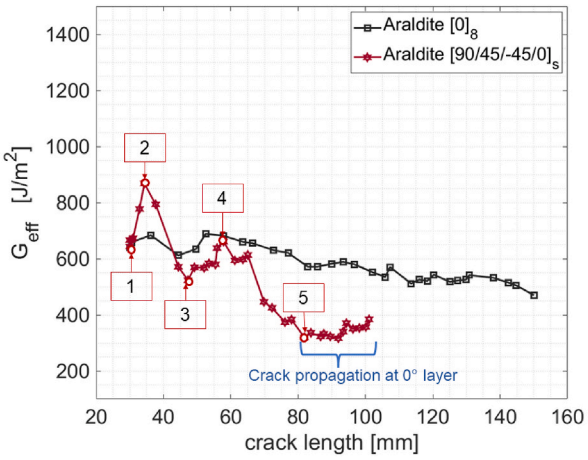

(a)

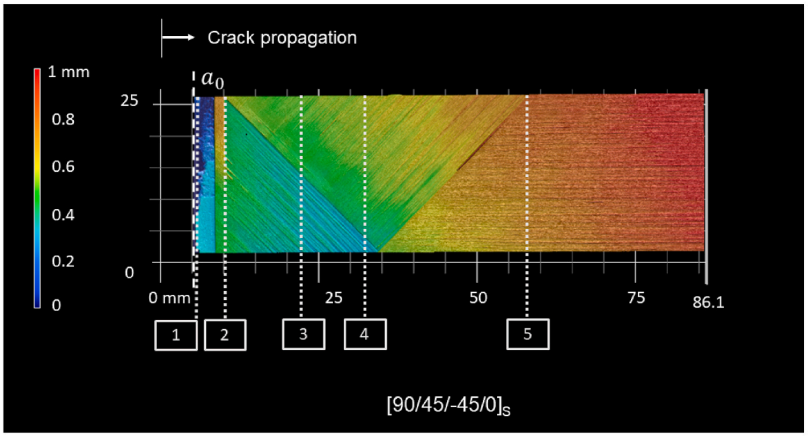

(b)

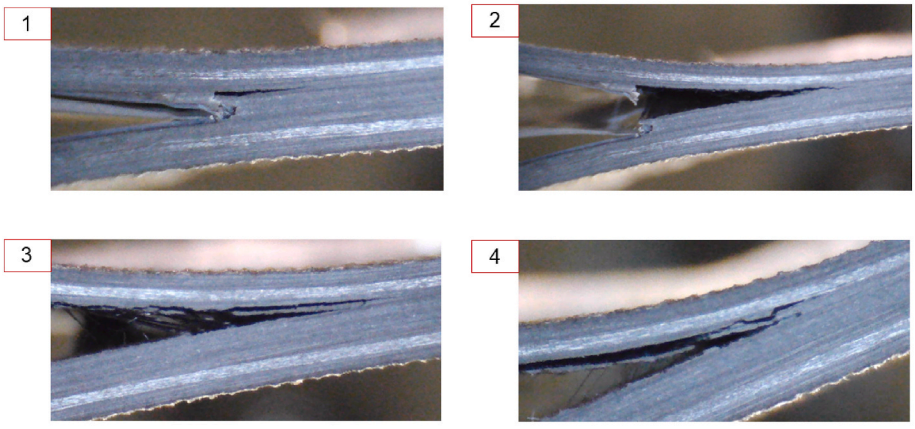

(c)

Fig. 15. (a) R-curve, (b) topography and (c) images taken by the travelling microscope of the specimen Araldite_[90/45/-45/0]s.

stresses that occur in the composite plies overcome the required stresses for fracture onset in the composite plies [30], propagating directly into the composite mid-plane instead of in the bondline. A similar figure is observed for the Araldite_[90/45/-45/0]$_S$. However, since we are in the presence of a less tough adhesive, it is also possible to see stiffness degradation at the CZE of the bondline and a preferential path for crack onset also within the bondline.

For the 60-degree laminates bonded with both adhesives, the adhesive type did not influence their damage mechanisms since the crack propagation occurred directly within the composite plies. Therefore, for these laminates, the geometric singularities created by the laminate stacking sequence represent a more decisive influence on the joint's

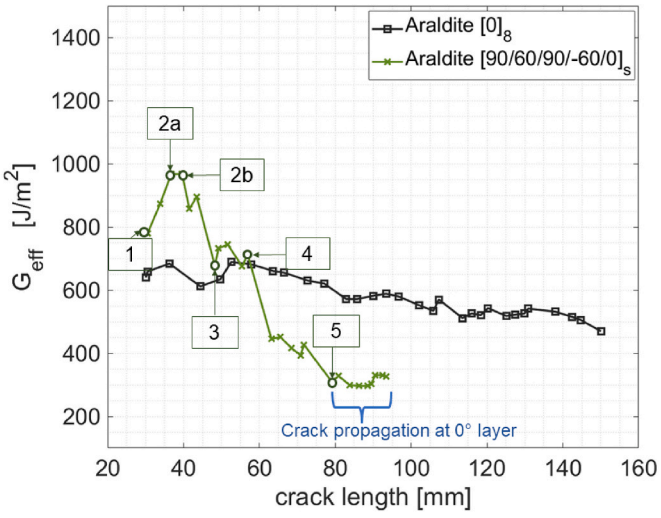

(a)

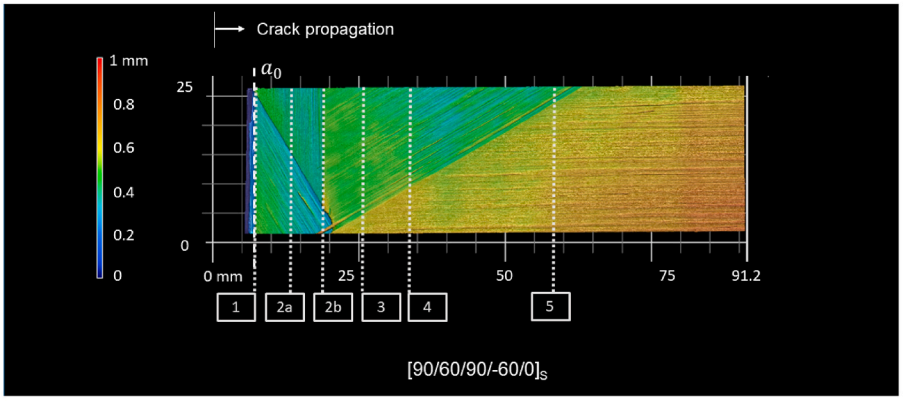

(b)

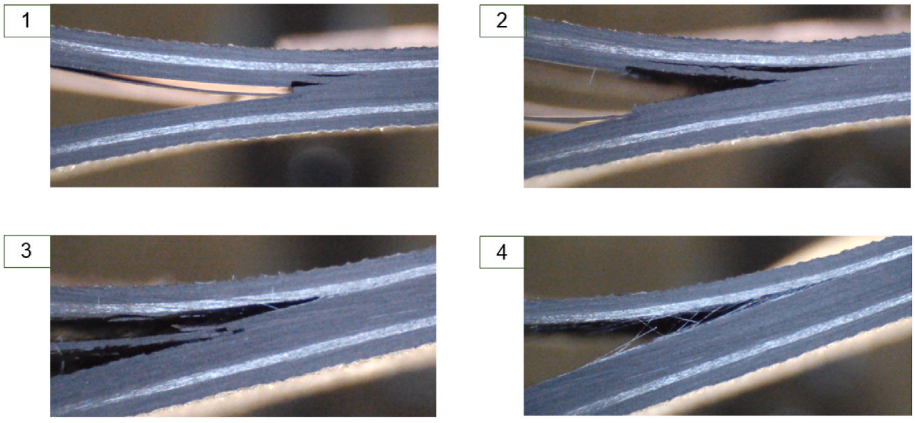

(c)

Fig. 16. (a) R-curve, (b) topography and (c) images taken by the travelling microscope of the specimen Araldite_[90/60/90/-60/0]s.

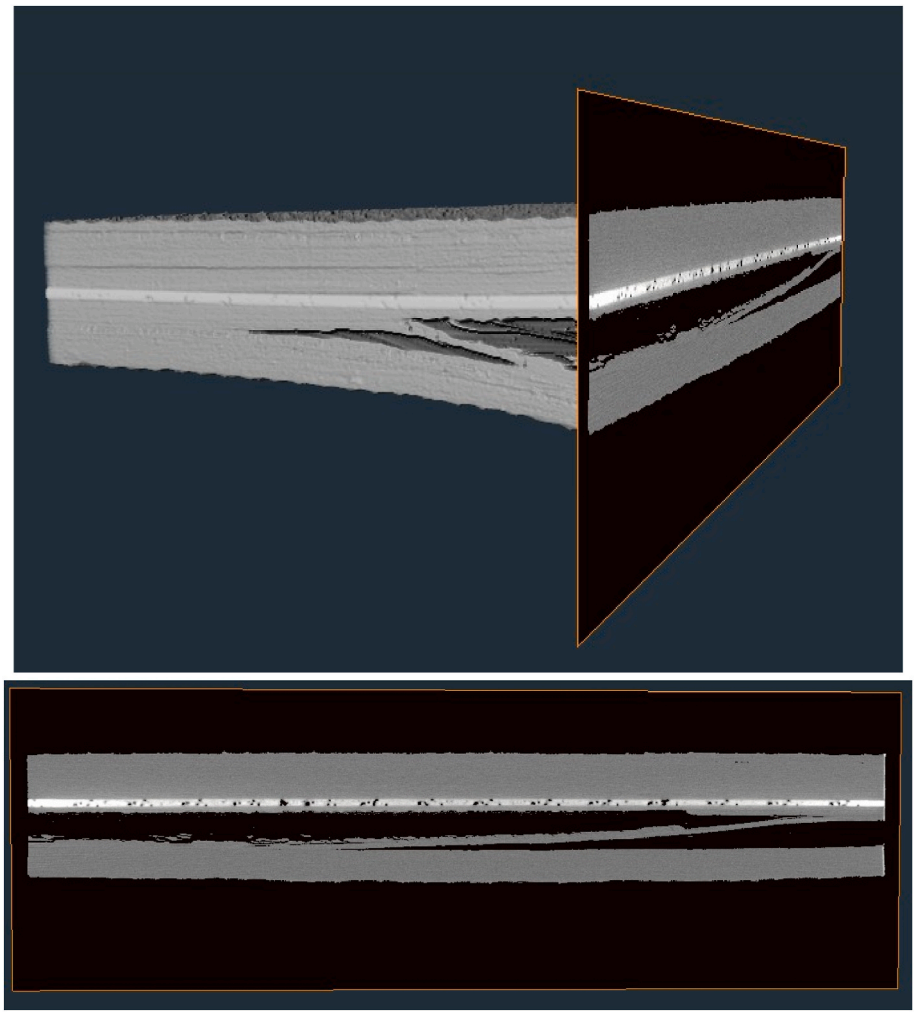

Fig. 17. Micro CT image of the Araldite_[90/60/90/-60/0]$_s$.

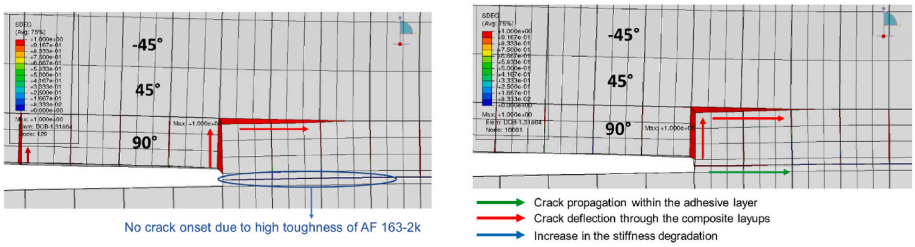

(a) AF 163-2k_[90/45/-45/0]s (b) Araldite_[90/45/-45/0]s

Fig. 18. CZE stiffness degradation for (a) AF163-2k_[90/45/-45/0]s and (b) Araldite_ [90/45/-45/0]s.

fracture mechanisms than the crack tip.

It was observed that once a matrix cracking occurs, it can keep propagating through the composite thickness or in the present interface (delamination), depending on the fibre orientation of the following layup. As also observed in previous works in the literature [11,29,38,45–48], when the following layup after a matrix cracking has a 0-degree orientation, small stresses singularities are present in a way that the more energetically favourable path for the crack propagates is the delamination at this interface.

Therefore, for the layups with 45 and 60-degree plies orientation, the crack mainly propagated through delamination simultaneously in different layers and multi-cracks that propagated through the composite's mid-plane until reaching the 0-degree ply, where the crack deflection stopped, and the crack stayed in the 0-degree delamination, as also observed in Ref. [47].

In conclusion, CFRP layup tailoring, combined with certain adhesive's mechanical properties, makes it possible to "play" with the geometric singularities within the joints and architect the fracture phenomena in the adhesive joint. Triggering crack competition mechanisms and multiple crack propagation through the composite's mid-plane can increase the joint's resistance against the crack onset. It is a possible direction to delay crack propagation further.

6. Conclusions

The effects of the CFRP layup on the crack propagation of adhesively bonded joints were studied. The possibility of enhancing the joint's fracture toughness by tailoring the CFRP layup was explored. Based on the results, the following conclusions can be drawn.

- CFRP adhesively bonded joints present complex failure mechanisms mainly triggered by crack deflections and crack competition between different crack locations. These fracture phenomena are influenced by the plies orientations and the stress singularities in the vicinity of the pre-crack tip;
- The fibre orientation of the first plies close to the bondline (interface plies) is crucial for the damage evolution within the bonded joints. 0-degree interface plies tend to prevent the crack deflection to the composite substrate since the adherents presented high stiffness compared to the other specimens. With the increase of the interface ply angle, the crack tends to propagate through the composite's mid-plane until reaching the following 0-degree ply, in which the crack propagates rapidly by complete delamination;
- Toughening mechanisms of crack deflection and crack competition observed in AF163-2k_[0/90_2/0]s enhance the fracture toughness at the crack onset by 10%. The triggering of these toughening mechanisms at the crack onset can only be achieved if the toughness of the adhesive is high enough not to be the preferred crack path.
- The layups with multi-fibre orientation angles (45°, 60° and 90°) triggered an increase in the joint's R-curve every time a crack deflected to a different ply. In the case of the low-toughness adhesive, the resulting fracture toughness of the joint surpassed the adhesive toughness, showing a promising solution to enhance the joint's resistance against crack propagation even after crack initiation and possibly delay crack growth.
- High-performance adhesives can trigger a crack competition mechanism that promotes crack deflection to a parallel layer. However, this can also result in a final brittle failure caused by delamination. New design possibilities are now open to achieve ultra-efficient composite bonded structures and repairing patches that can benefit from these migrations.

In summary, three toughening mechanisms could be achieved by architecting the composite substrates layup.

- At crack onset: substrates with cross-ply laminates in combination with high-toughness adhesives trigger crack competition resulting in an increase of 10% at the crack onset region compared with pure cohesive failure.
- During crack propagation: 0° substrates in combination with adhesives with embedded meshes trigger cohesive failure with carrier bridging, increasing 16 J/m^2 toughness with every increment of the crack.
- At the crack onset and during crack propagations: multidirectional laminates in combination with low-toughness adhesive trigger crack deflections within the laminate that has the potential to surpass the adhesive toughness. An increase of around 15% and 37% of the effective fracture toughness onset of the Araldite_$[90/45/-45/0]_S$ and Araldite_$[90/60/90/-60/0]_S$ joints when compared to pure cohesive failure. Moreover, the crack deflection and multiple crack propagations lead to peaks of the effective fracture toughness, resulting in an increase of 37% and 100% of the Araldite_$[90/45/-45/0]_S$ and Araldite_$[90/60/90/-60/0]_S$ joints when compared with the average value observed on the Araldite_$[0]_8$.

Author statement

R. A. A. Lima: Methodology; Investigation; Writing - Original Draft; Visualization. R. Tao:; Methodology; Investigation; Writing - Review & Editing. A. Bernasconi: Writing - Review & Editing; Supervision. M. Carboni: Writing - Review & Editing; Supervision. N. Carrere: Conceptualization; Methodology; Writing - Review & Editing; Supervision. S. Teixeira de Freitas: Conceptualization; Methodology; Writing - Original Draft; Visualization; Supervision.

Declaration of competing interest

The authors declare that they have no known competing financial interests or personal relationships that could have appeared to influence the work reported in this paper.

Data availability

Data will be made available on request.

Acknowledgements

This article is based upon work from COST Action CA18120 (CERTBOND - https://certbond.eu/), supported by COST (European Cooperation in Science and Technology).

The authors would like to acknowledge the support for the experimental and numerical analysis of the Master's students: Nicholas Rox and Akshit Oswal, from the ENSTA Bretagne.

References

[1] Marques AC, Mocanu A, Tomić NZ, Balos S, Stammen E, Lundevall A, Abrahami ST, Günther R, de Kok JMM, de Freitas ST. Review on adhesives and surface treatments for structural applications: recent developments on sustainability and implementation for metal and composite substrates. Materials 2020;13(24):1–43. https://doi.org/10.3390/ma13245590.

[2] Banea MD, da Silva LFM. Adhesively bonded joints in composite materials: an overview. Proc Inst Mech Eng Part L 2009;223(1):1–18. https://doi.org/10.1243/14644207JMDA219.

[3] Tao R, Li X, Yudhanto A, Alfano M, Lubineau G. Laser-based interfacial patterning enables toughening of CFRP/epoxy joints through bridging of adhesive ligaments. Composer Part A Appl Sci Manuf 2020;139(September):106094. https://doi.org/10.1016/j.compositesa.2020.106094.

[4] Jeevi G, Kumar Nayak S, Abdul Kader M. Review on adhesive joints and their application in hybrid composite structures. J Adhes Sci Technol 2019;33:1497–520. https://doi.org/10.1080/01694243.2018.1543528.

[5] Tserpes K, Barroso-Caro A, Carraro PA, Beber VC, Floros I, Gamon W, Kozłowski M, Santandrea F, Shahverdi M, Skejić D, Bedon C, Rajčić V. A review on failure theories and simulation models for adhesive joints. J Adhes 2021;00(00):1–61. https://doi.org/10.1080/00218464.2021.1941903.

[6] Viana G, Costa M, Banea MD, da Silva LFM. A review on the temperature and moisture degradation of adhesive joints. Proc Inst Mech Eng Part L 2017;231(5):488–501. https://doi.org/10.1177/1464420716671503.

[7] Kadlec M, Růžek R, Bělský P. Concurrent use of Z-pins for crack arrest and structural health monitoring in adhesive-bonded composite lap joints. Compos Sci Technol December 2019;188:2020. https://doi.org/10.1016/j.compscitech.2019.107967.

[8] Ruairidh A, Droubi MG, Haque N, August F. Defect detection and condition assessment of adhesively-bonded joints using acoustic emission. 2021. August.

[9] Heller K, Jacobs LJ, Qu J. Characterisation of adhesive bond properties using Lamb waves. NDT E Int 2000;33(8):555–63. https://doi.org/10.1016/S0963-8695(00)00022-0.

[10] Dwivedi SK, Vishwakarma M, Soni PA. Advances and researches on non destructive testing: a review. Mater Today Proc 2018;5(2):3690–8. https://doi.org/10.1016/j.matpr.2017.11.620.

[11] Kupski J, Zarouchas D, Teixeira de Freitas S. Thin-plies in adhesively bonded carbon fiber reinforced polymers. Compos B Eng 2020;184:107627. https://doi.org/10.1016/j.compositesb.2019.107627.

[12] Daynes S, Weaver PM. Stiffness tailoring using prestress in adaptive composite structures. 2013. https://doi.org/10.1016/j.compstruct.2013.05.059.

[13] Eisenhut D, Moebs N, Windels E, Bergmann D, Geiß I, Reis R, Strohmayer A. Aircraft Requirements for Sustainable Regional Aviation 2021. https://doi.org/10.3390/aerospace8030061.

[14] Budzik M, Jumel J, Imielińska K, Shanahan MER. Fracture in composite/aluminium joints of variable adhesive properties. J Adhes 2009;85(10):736–54. https://doi.org/10.1080/00218460902997232.

[15] Tao R, Li X, Yudhanto A, Alfano M, Lubineau G. On controlling interfacial heterogeneity to trigger bridging in secondary bonded composite joints: an efficient strategy to introduce crack-arrest features. Compos Sci Technol 2020;188(December 2019):107964. https://doi.org/10.1016/j.compscitech.2019.107964.

[16] Wagih A, Tao R, Yudhanto A, Lubineau G. Improving mode II fracture toughness of secondary bonded joints using laser patterning of adherends. Composer Part A

Appl Sci Manuf 2020;134(April):105892. https://doi.org/10.1016/j.compositesa.2020.105892.
[17] Teixeira de Freitas S, Zarouchas D, Poulis JA. The use of acoustic emission and composite peel tests to detect weak adhesion in composite structures. J Adhes 2018;94(9):743–66. https://doi.org/10.1080/00218464.2017.1396975.
[18] Hu P, Pulungan D, Tao R, Lubineau G. Influence of curing processes on the development of fiber bridging during delamination in composite laminates. Compos Appl Sci Manuf 2021;149. https://doi.org/10.1016/j.compositesa.2021.106564.
[19] Güemes A, Renato Pozo-Morales A, Fernandez-Lopez A, Sánchez-Romate XF, Sánchez M, Ureña A. Strain and damage sensing by CNT modified adhesive films and fiber optic distributed sensing. Comparison of performances in a double lap bonded joint. 2019. p. 1–6 [Online]. Available: http://www.ndt.net/?id=25035.
[20] Yoon SH, Lee DG. In situ crack propagation monitoring in tubular adhesive joints containing quartz nanoparticles. J Adhes Sci Technol 2011;25(16):1973–85. https://doi.org/10.1163/016942410X544776.
[21] Kinloch AJ, Lee JH, Taylor AC, Sprenger S, Eger C, Egan D. The Journal of Adhesion Toughening structural adhesives via nano-and micro-phase inclusions. 2010. https://doi.org/10.1080/00218460309551.
[22] Quan D, Murphy N, Ivankovic A. Fracture behaviour of a rubber nano-modified structural epoxy adhesive: bond gap effects and fracture damage zone. Int J Adhesion Adhes 2017;77(May):138–50. https://doi.org/10.1016/j.ijadhadh.2017.05.001.
[23] Rao Q, Ouyang Z, Peng X. Enhancing mode I fracture toughness of adhesively bonded unidirectional composite joints using surfactant-stabilised multi-walled carbon nanotube and graphene nanoplate. Polym Test Apr. 2021;96. https://doi.org/10.1016/J.POLYMERTESTING.2021.107110.
[24] Buchman A, Dodiuk-Kenig H, Dotan A, Tenne R, Kenig S. Toughening of epoxy adhesives by nanoparticles. J Adhes Sci Technol 2009;23(5):753–68. https://doi.org/10.1163/156856108X379209.
[25] Carbas RJC, da Silva LFM, Andrés LFS. Functionally graded adhesive joints by graded mixing of nanoparticles. Int J Adhesion Adhes Jul. 2017;76:30–7. https://doi.org/10.1016/J.IJADHADH.2017.02.004.
[26] D. Quan, N. Murphy, S. Flynn, M. Artuso, C. Rouge, and A. Ivanković, "Interlaminar fracture toughness of CFRPs interleaved with stainless steel fibres Combining deep learning with computational continuum mechanics (SmartSim) View project Surrogate Lung View project Interlaminar fracture toughness of CFRPs interleaved with stainless steel fibres", doi: 10.1016/j.compstruct.2018.11.016.
[27] Minakuchi S, Takeda N. Arresting crack in composite bonded joint under fatigue using fiber-reinforcement-based feature. International SAMPE Technical Conference; 2017. p. 199–206. August.
[28] M. Frascio, E. A. S. Marques, R. J. C. Carbas, L. F. M. Da Silva, M. Monti and M. Avalle , "Review of tailoring methods for joints with additively manufactured adherends and adhesives", doi: 10.3390/ma13183949.
[29] Khan MA. Development of rules for the design of adhesively bonded fibre-reinforced plastic composite joints in aerospace applications. 2018.
[30] Lopes Fernandes R, Teixeira de Freitas S, Budzik MK, Poulis JA, Benedictus R. From thin to extra-thick adhesive layer thicknesses: fracture of bonded joints under mode I loading conditions. Eng Fract Mech Sep. 2019;218. https://doi.org/10.1016/J.ENGFRACMECH.2019.106607.
[31] Kupski J, Teixeira de Freitas S, Zarouchas D, Camanho PP, Benedictus R. Composite layup effect on the failure mechanism of single lap bonded joints. Compos Struct Jun. 2019;217:14–26. https://doi.org/10.1016/J.COMPSTRUCT.2019.02.093.
[32] Ozel A, Yazici B, Akpinar S, Aydin MD, Temiz Ş. A study on the strength of adhesively bonded joints with different adherends. Compos B Eng Jun. 2014;62:167–74. https://doi.org/10.1016/J.COMPOSITESB.2014.03.001.
[33] Burns LA, Mouritz AP, Pook D, Feih S. Strength improvement to composite T-joints under bending through bio-inspired design. Composer Part A Appl Sci Manuf Nov. 2012;43(11):1971–80. https://doi.org/10.1016/J.COMPOSITESA.2012.06.017.
[34] HexPly ® 8552 Epoxy matrix (180°C/356°F curing matrix). 2020.
[35] Standard test method for mode I interlaminar fracture toughness of unidirectional fiber-reinforced polymer matrix composites. https://www.astm.org/d5528-13.html. [Accessed 10 September 2022].
[36] BS ISO 25217. Adhesives — determination of the mode I adhesive fracture energy of structural adhesive joints using double cantilever beam and tapered double cantilever beam specimens. 2009. https://www.iso.org/standard/42797.html. April, 2023.
[37] Turon A, Costa J, Camanho PP, Dávila CG. Simulation of delamination in composites under high-cycle fatigue. Composer Part A Appl Sci Manuf 2007;38(11):2270–82. https://doi.org/10.1016/j.compositesa.2006.11.009.
[38] Kupski J, Teixeira de Freitas S, Zarouchas D, Camanho PP, Benedictus R. Composite layup effect on the failure mechanism of single lap bonded joints. Compos Struct Jun. 2019;217:14–26. https://doi.org/10.1016/J.COMPSTRUCT.2019.02.093.
[39] Araldite ® 2015-1 Two component epoxy paste adhesive Key properties [Online], www.araldite adhesives.com. [Accessed 10 September 2022].
[40] Lavalette Nicolas P, Bergsma Otto K. Dimitrios Zarouchas, Rinze Benedictus, Influence of geometrical parameters on the strength of Hybrid CFRP-aluminium tubular adhesive joints. Compos Struct 2020;240. https://doi.org/10.1016/j.compstruct.2020.112077.
[41] Heide-Jørgensen S, de Freitas ST, Budzik MK. On the fracture behaviour of CFRP bonded joints under mode I loading: effect of supporting carrier and interface contamination. Compos Sci Technol 2018;160. https://doi.org/10.1016/j.compscitech.2018.03.024.
[42] Moroni F, Pirondi A, Pernechele C, Vescovi L. Comparison of tensile strength and fracture toughness of Co-bonded and cold-bonded carbon fiber laminate-aluminum adhesive joints. Materials 2021;14:3778. https://doi.org/10.3390/ma14143778.
[43] Bach C, Jebari R, Viti A, Hewson R. Composite stacking sequence optimisation for aeroelastically tailored forward-swept wings. Struct Multidiscip Optim Jan. 2017;55(1):105–19. https://doi.org/10.1007/S00158-016-1477-3/METRICS.
[44] Saleh MN, Budzik MK, Saeedifar M, Zarouchas D, De Freitas ST. On the influence of the adhesive and the adherend ductility on mode I fracture characterisation of thick adhesively-bonded joints. Int J Adhesion Adhes 2022;115. https://doi.org/10.1016/j.ijadhadh.2022.103123.
[45] Davidson BD, Krüger R, König M. Effect of stacking sequence on energy release rate distributions in multidirectional DCB and ENF specimens. Eng Fract Mech 1996;55(4):557–69. https://doi.org/10.1016/S0013-7944(96)00037-9.
[46] Abd Rased MF, Yoon SH. Experimental study on effects of asymmetrical stacking sequence on carbon fiber/epoxy filament wound specimens in DCB, ENF, and MMB tests. Compos Struct 2021;264. https://doi.org/10.1016/j.compstruct.2021.113749.
[47] Aydin MD. 3-D nonlinear stress analysis on adhesively bonded single lap composite joints with different ply stacking sequences, vol. 84; Jan. 2008. p. 15–36. https://doi.org/10.1080/00218460801888359. 1.
[48] Purimpat S, Jérôme R, Shahram A. Effect of fiber angle orientation on a laminated composite single-lap adhesive joint, vol. 22; Jun. 2013. p. 139–49. https://doi.org/10.1080/09243046.2013.782805. 3.